Photocatalytic degradation of industrial pulp and paper mill effluent using synthesized magnetic Fe_2O_3-TiO_2: Treatment efficiency and characterizations of reused photocatalyst

Wennie Subramonian, Ta Yeong Wu* and Siang-Piao Chai

Chemical Engineering Discipline, School of Engineering, Monash University, Jalan Lagoon Selatan, 47500 Bandar Sunway, Selangor Darul Ehsan, Malaysia.

*Corresponding author: Ta Yeong Wu

E-mail addresses: wu.ta.yeong@monash.edu; tayeong@hotmail.com

Tel.: +60 3 55146258

Fax.: +60 3 55146207

ABSTRACT

In this work, treatment of pulp and paper mill effluent (PPME) was studied by means of heterogeneous photocatalysis. Magnetically retrievable Fe_2O_3-TiO_2 was fabricated by employing a solvent-free mechanochemical process under ambient conditions. Findings elucidated the successful incorporation of Fe_2O_3 into the TiO_2 lattice. Fe_2O_3-TiO_2 was found to be an irregular and slightly agglomerated surface morphology. In comparison to commercial P25, Fe_2O_3-TiO_2 exhibited higher ferromagnetism and enhanced catalyst properties in terms of specific surface area (58.40 m^2/g), pore volume (0.29 cm^3/g), pore size (18.52 nm), and band gap (2.95 eV). Besides, reusability study revealed that Fe_2O_3-TiO_2 was chemically stable and could be reused successively (five cycles) without significant change in its photoactivity and intrinsic properties. Additionally, this study demonstrated the potential recovery of Fe_2O_3-TiO_2 from an aqueous suspension by using an applied magnetic field or sedimentation. Interactive effects of photocatalytic conditions (initial effluent pH, Fe_2O_3-TiO_2 dosage, and air flow-rate), reaction mechanism, and the presence of chemical oxidants (H_2O_2, BrO_3^-, and ClO^- ions) during treatment were also investigated. Under optimal conditions (initial effluent pH = 3.88, [Fe_2O_3-TiO_2] = 1.3 g/L, and air flow-rate = 2.28 L/min), the treatment efficiency of Fe_2O_3-TiO_2 was 98.5% higher than P25. Based on Langmuir-Hinshelwood kinetic model, apparent rate constants of Fe_2O_3-TiO_2 and P25 were 9.2 x 10^{-3} and 2.7 x 10^{-3} min^{-1}, respectively. The present study revealed that the effective treatment of PPME using magnetic Fe_2O_3-TiO_2 showed high reusability and easy separation of photocatalyst from the wastewater.

Keywords: Magnetic Fe_2O_3-TiO_2; Mechanochemical milling; Green synthesis; Photocatalysis; Response surface methodology; Wastewater treatment

1. Introduction

In recent years, the pulp and paper industry in Malaysia has doubled its production capacity (MIDA, 2015). To date, there are 23 operating pulp and paper mills with a total production capacity of 1.3 million tons per annum (Hay et al., 2016). Among the industries, pulp and paper industry generates the third largest amount of wastewater after primary metals and chemical industries (Ashrafi et al., 2015). The World Bank Group (2007) reported a discharge of 10-250 m^3 of wastewater per ton of product manufactured. Pulp and paper mill effluent (PPME) primarily consists of various organic and inorganic pollutants such as tannins, lignins, resins, chlorinated phenol compounds, suspended solids, diterpene alcohols, waxes, and fatty acids (Hermosilla et al., 2015). These pollutants contribute to high total suspended solids (TSS) and chemical oxygen demand (COD) in the PPME (Ashrafi et al., 2015). Moreover, such effluent generated from various pulp and paper-making stages adversely affects the receiving aquatic environment through slime production, scum formation, thermal impact, and carcinogenic risk to exposed communities (Kamali et al., 2015). Clearly, PPME is a source of grave environmental concern, thus, highlighting the importance in developing an effective wastewater treatment strategy in the pulp and paper industry.

Biological process is commonly applied in treatment of real wastewater, including PPME. However, conventional biological methods generate large volume of sludge, have low colour removal, and are incapable of degrading complex, high molecular weight and bio-recalcitrant contaminants (Hay et al., 2015; Hermosilla et al., 2015). Alternately, advanced oxidation processes have become an alternative approach to effectively oxidize most recalcitrant pollutants into carbon dioxide and water due to generation of highly reactive hydroxyl radicals (·OH)

(Khodami and Nezamzadeh-Ejhieh, 2015; Visa et al., 2015). Additionally, other advantages of advanced oxidation processes include colour removal, lower sludge production, and simple to operate (Chin et al., 2016). Over the past decade, heterogeneous photocatalysis has garnered much attention among other advanced oxidation processes. Accordingly, the use of TiO_2 in photocatalysis has emerged as a leading choice because of its superior redox potentials, chemical inertness, long term thermodynamic stability, non-toxicity, high photoactivity, inexpensiveness, and environmentally benign nature (Cao et al., 2015). Albeit its advantages, TiO_2 has a wide band gap and a high recombination rate of photogenerated electron-hole pairs (Zangeneh et al., 2015). To overcome these limitations, it is necessary to modify TiO_2 to enhance its photocatalytic activity in this study.

Numerous past studies have reported promising results in coupling metal oxides with TiO_2 to attain higher photoactivity due to difference in band gaps of the two metal oxides (Patra et al., 2012). Nevertheless, issues of catalyst recovery and reuse from wastewater remain as major setbacks in practical treatment process (Yao et al., 2015). To address these issues, magnetic separation using an external magnetic field is a useful recovery method since it is faster and more efficient as compared to filtration and decantation (Pang et al., 2014; Cao et al., 2015). Besides, magnetic separable catalysts were reported to have good dispersion in reaction suspension, high mechanical stability, and desirable paramagnetic nature for easy separation and reuse (Bhosale et al., 2015). Recently, iron-containing catalysts have attracted wide interest since it is less toxic to the environment as compared to the late-transition metals (Patra et al., 2012). In particular, photocatalysts consisting of iron oxide compounds (Fe_2O_3 and Fe_3O_4) are preferred as they are inexpensive, abundant, easy to prepare, highly magnetic, and they enhance photocatalytic activity by promoting interface charge transfer in hetero-structured materials (Qin et al., 2014;

Cao et al., 2015). Based on the aforementioned advantages, Fe_2O_3 was selected in this work to couple with TiO_2. The current study adopted mechanochemical process/mechanical milling as a prospective Fe_2O_3-TiO_2 synthesis route. This synthesis method omits the use of volatile organic solvents, toxic reagents, and harsh reaction conditions (Bhosale et al., 2015).

Currently, the latest research not only emphasized on the development of simple and green routes for catalyst fabrication, but also focused on the practical application of the synthesized catalyst (Bhosale et al., 2015). Thus, the primary objective of the present work was to effectively degrade real PPME using a magnetically retrievable and reusable photocatalyst synthesized from an environmentally friendly and facile process. Herein, (i) modeling and interactive influence of photocatalytic operating conditions (initial effluent pH, Fe_2O_3-TiO_2 dosage, and air flow-rate) by using response surface methodology (RSM), (ii) kinetic study and photocatalytic reaction mechanism, (iii) role of reactive oxidants during photocatalysis, (iv) reusability and retrieval of Fe_2O_3-TiO_2, and (v) characteristics of the fresh and reused Fe_2O_3-TiO_2 were reported in this study. To the best of our knowledge, the use of mechanically milled photocatalyst to photodegrade real industrial wastewater, including PPME, has yet to be reported.

2. Experimental details

2.1. Materials

Iron (III) oxide powder, Aeroxide® P25, anatase titanium (IV) oxide, rutile titanium (IV) oxide, and potassium bromate were purchased from Sigma-Aldrich whereas hydrogen peroxide (35%) and sodium hypochlorite (6-14% active chlorine) were procured from Merck Millipore. The chemicals were used as received. Raw PPME was collected from Muda Paper Mills Sdn.

Bhd., Selangor and was stored at 4 °C to reduce biological degradation. Raw PPME was then pre-treated via coagulation process based on the methodology suggested by Subramonian et al. (2015). Typically, coagulation-flocculation process is regarded as one of the most important and widely used (pre)treatment process of industrial wastewater due to its simplicity and effectiveness (Teh et al., 2016). In this study, *Cassia obtusifolia* seed gum was used as a natural coagulant to pre-treat raw and undiluted PPME (Subramonian et al., 2014). The coagulation-flocculation process was needed to reduce light scattering effect during photocatalysis, which was caused by high loading of TSS present in the raw PPME.

2.2. Green synthesis of magnetic Fe_2O_3-TiO_2

A stoichiometric mixture of Fe_2O_3 (1 mol%) and P25 powder was mechanochemically milled in a planetary ball mill (Fritsch Pulverisette 5) under solvent-free and ambient conditions to produce Fe_2O_3-TiO_2 photocatalyst. Mechanical milling was performed up to 20 min using 250 rpm and ball to powder mass ratio of 10:1 in zirconia vials. The fabricated Fe_2O_3-TiO_2 was subjected to characterization and photodegradation studies of PPME.

2.3. Characterization study

Ultraviolet-visible (UV-vis) diffused reflectance spectra of the samples were recorded on a UV-vis spectroscopy (Cary 100, Agilent). Subsequently, band gap energies of the samples were determined from transformed Kubelka-Munk function $[F(R)\cdot h\nu]^{1/2}$ against the abscissa of photon energy ($h\nu$) plot. Meanwhile, textural properties of samples were evaluated based on nitrogen adsorption/desorption isotherms using Micromeritics, ASAP 2020. Specific surface areas and pore distributions were calculated from Brunauer-Emmett-Teller (BET) and Barrett-Joyner-

Halenda (BJH) methods, respectively. Surface morphology of the samples was observed using a field electron scanning electron spectroscopy (FESEM) (Hitachi SU8010). Raman analysis was conducted using HORIBA Scientific, LabRAM HR Evolution with an excitation wavelength of 514 nm at room temperature whereas Fourier transform infrared (FTIR) spectra were recorded on a FTIR spectrophotometer (Thermo Scientific Nicolet iS10) over a range of 4000-400 cm^{-1} at room temperature. Meanwhile, magnetic properties of samples were measured using a vibrating sample magnetometer, VSM (7404, LakeShore) whereas thermogravimetric analysis (TGA) was carried out from room temperature to 900 °C with 10 °C min^{-1} heating rate under N_2 atmosphere (TGA/ SDTA 851, Mettler Toledo). Lastly, zeta potential of samples was measured using a zetasizer (Malvern Zetasizer Nano-ZS).

2.4. Photodegradation of PPME using Fe_2O_3-TiO_2

In a typical photodegradation procedure, an appropriate amount of Fe_2O_3-TiO_2 was dispersed in 50 mL of PPME adjusted to a desired initial pH value. Suspension was then magnetically stirred in the dark at 800 rpm for 30 min to achieve adsorption-desorption equilibrium. The mixture was then irradiated with a 400 W UV lamp for 3 h under continuous aeration and stirring. Initial effluent pH, Fe_2O_3-TiO_2 dosage, and air flow-rate were adjusted to the values as proposed by RSM in Table 1. The initial and final samples were withdrawn from the suspension before and after irradiation to calculate a change in COD value (Eq. (1)). Photocatalyst was removed from the samples by centrifugation at 13500 rpm for 15 min.

$$COD\ \ removal, \% = \frac{COD_{initial} - COD_{final}}{COD_{initial}} \times 100 \qquad (1)$$

2.5. Experimental design

Conventional statistical approach of varying one-variable-at-a-time while other process parameters are held constant does not consider interaction among parameters (Subramonian et al, 2015). Additionally, one-variable-at-a-time technique is a time consuming method and involves large number of experiments (Wu et al., 2009; Shak and Wu, 2015). Therefore, RSM technique was used to develop a regression model equation, which was useful in optimizing the photocatalytic operating conditions and to better understand the interdependent relations between these parameters (Debnath et al., 2015). In order to achieve this, RSM was performed by employing a central composite design (CCD). CCD is the most common form to determine a mathematical model based on a reduced number of experimental runs (Fathinia et al., 2015) and it was proven in our previous work to be an efficient design tool to fit second-order models (Teh et al., 2014; Subramonian et al., 2015). Combined influence of initial pH of PPME, Fe_2O_3-TiO_2 dosage, and air flow-rate (independent variables) on the photodegradation efficiency (response) was evaluated. Range and coded levels of the independent variables are presented in Table 1. A total of 20 experimental runs were conducted and a general form of second-order polynomial quadratic model was used to describe the influence of independent variables on the response as described in Eq. (2) (Hay et al., 2012; Zhong et al., 2014):

$$Y = \beta_0 + \sum_{i=1}^{k} \beta_i X_i + \sum_{i=1}^{k} \beta_{ii} X_i^2 + \sum_{i<j} \beta_{ii} X_i X_j \qquad (2)$$

where Y = responses (COD removal); β_0 = constant; β_i = linear coefficient; β_{ii} = quadratic coefficient; β_{ij} = interactive coefficient; X_i and X_j = actual factor level. Interactive effects between the independent variables and response were also represented as 3-D response surface

plots. Computational analysis of the experimental data was carried out using Design-Expert® software (Version 6.0.10, Stat-Ease Inc. Minneapolis, USA).

2.6. Reusability and retrieval of Fe_2O_3-TiO_2

Reusability and stability of the fabricated Fe_2O_3-TiO_2 photocatalyst was further examined under optimal photocatalytic conditions. After completion of a photocatalytic run, the photocatalyst was separated from the PPME suspension through simple filtration. The photocatalyst was later washed thoroughly with deionized water and dried overnight at 60 °C before subjecting to subsequent runs. Reuse of Fe_2O_3-TiO_2 was conducted for several cycles. Retrieval of Fe_2O_3-TiO_2 from the deionized water was examined using a household permanent magnet. The reused Fe_2O_3-TiO_2 was characterized using BET and BJH methods, FESEM, Raman spectroscopy, FTIR spectrophotometer, and VSM as proposed in Section 2.3.

3. Results and discussion

3.1. Comparison among control experiments and Fe_2O_3-TiO_2

Prior to the development of experimental design using RSM, several control experimental runs were conducted and the results are depicted in Table 2. Noticeably, photodegradation solely due to UV irradiation (photolysis) and adsorption of pollutants onto Fe_2O_3-TiO_2 photocatalyst (catalysis) were negligible (0.1 and 0.4% of COD removal, respectively). On the other hand, photodegradation using mechanically milled Fe_2O_3-TiO_2 (62.3% of COD removal) was higher

than the commercial P25, anatase TiO_2, rutile TiO_2, and Fe_2O_3 (40.6, 24.9, 2.9, and 1.1% of COD removal, respectively). Notably, coupling of Fe_2O_3 with TiO_2 promoted better light harvesting ability and optical properties in accordance with the reduced band gap (2.95 eV) of Fe_2O_3-TiO_2 as compared to P25 (3.35 eV) in Fig. 1. The lower band gap of Fe_2O_3-TiO_2 was due to electronic coupling between the wide band gap of TiO_2 and narrow band gap of Fe_2O_3 (Wang et al., 2013).

In order to ensure economic optimization of the treatment process, extent of UV irradiation time to photodegrade PPME was also evaluated (Gimeno et al., 2016). Fig. 2 depicts an improvement in photodegradation (0 to 62.5% of COD removal) when irradiation time increased from 0 to 5 h. However, there was no significant improvement in photocatalysis after 3 h due to deactivation of Fe_2O_3-TiO_2 active sites by strong deposition of by-products (Zangeneh et al., 2015). Therefore, the maximum irradiation time of 3 h was kept constant for all subsequent experimental runs.

3.2. RSM modeling and optimization study on photocatalysis of PPME

Photocatalytic reactions depend on a multitude of operating conditions. Initial effluent pH, Fe_2O_3-TiO_2 dosage, and air flow-rate were selected as treatment conditions in this optimization study. Based on a three-factor CCD matrix using RSM, quadratic model in terms of actual factors is expressed as follow:

$$COD\ removal = -377.79 + 177.69X_1 - 30.65X_2 + 104.21X_3 - 23.48X_1^2 - 16.20X_2^2 - 31.92X_3^2 + 5.21X_1X_2 + 34.72X_2X_3 \quad (3)$$

where X_1, X_2, and X_3 represented initial pH (of the effluent), photocatalyst (Fe_2O_3-TiO_2) dosage, and air flow-rate, respectively. A positive sign of regression coefficients denoted that the variable had a synergistic effect on the response (COD removal) whereas a negative sign signified an antagonistic effect on the response (Debnath et al., 2015). Variable with the largest regression coefficient magnitude was initial effluent pH, signifying that pH was the most dominant factor in the overall response. In order to test the significance and adequacy of the predicted quadratic model (Eq. (3)), analysis of variance (ANOVA) regression parameters (Table 3) were evaluated. *p* value is used to estimate whether *F* value is large enough to indicate statistical significance (Sridhar et al., 2014). Values of *p* less than 0.05 implied that the quadratic model terms are significant (Brzozowski and Lewandowska, 2014). ANOVA results confirmed that all of the tested operating conditions and quadratic model were highly significant with *p* values less than 0.05. The obtained adequate precision value (67.16) was greater than 4, verifying adequate signal for the model to navigate the design space (Soleymani et al., 2015). Lack-of-fit test described variation of data around the fitted model (Subramonian et al., 2015). The model had insignificant lack-of-fit values, which supported a strong model correlation between the operating conditions and COD removal. Additionally, R^2 value greater than 0.75 indicates the aptness of the model (Naik and Setty, 2014) and adjusted R^2 indicates the capability of the developed model to satisfactorily describe the system behaviour within the range of operating factors (Bhanarkar et al., 2014). In this study, the quadratic model was well-fitted to the experimental data with high R^2 and adjusted R^2 values (0.9966 and 0.9935, respectively).

3-D response surface plots (Fig. 3) were useful to reveal the influence of the independent variables (initial pH, Fe_2O_3-TiO_2 dosage, and air flow-rate) on the response (COD removal). Solubility and stability of the organic impurities were essentially dependent on the pH of the

medium (Das et al., 2014). In addition, pH also determined the electrostatic interaction of Fe_2O_3-TiO_2 surface, charged radicals formed during photocatalysis, and target pollutants (Khodami et al., 2015). Thus, variation of pH played a critical role in controlling photocatalytic efficiency. In this study, COD removal drastically decreased with increasing pH. This was due to undesirable electrostatic repulsion between negatively charged Fe_2O_3-TiO_2 surface and negatively charged organic pollutants at higher pH. Moreover, the presence of OH^- in excess hindered the formation of ·OH at higher pH (Debnath et al., 2015). On the contrary, COD removal improved tremendously when the pH shifted towards acidic region (Fig. 3a and b). At acidic conditions, Fe_2O_3-TiO_2 catalyst surface carried a net positive charge, while the organic pollutants were negatively charged. This promoted better adsorption, which led to higher photodegradation efficiency (Bhattacharjee et al., 2015). Similar findings were reported by Hassan et al. (2016) that the removal of organic pollutants using photocatalysis was favourable under acidic conditions as compared to neutral or alkaline conditions.

Determination of optimum dosage was paramount to minimize economic cost while achieving desirable treatment efficiency (Subramonian et al., 2014; Fathinia et al., 2015). Findings showed that COD removal gradually improved with increasing dosage (Fig. 3a and c). The increase in dosage led to a direct increase in catalyst active sites, which in turn, promoted increases in both ·OH and superoxide radical anion ($O_2^{\cdot -}$) generations (Debnath et al., 2015; Khodami et al., 2015). Conversely, excessive addition of Fe_2O_3-TiO_2 beyond optimum dosage caused an increase in turbidity of the wastewater, which led to light scattering effect and lower degradation efficiency (Low et al., 2012; Hassan et al., 2016). It was also reported that particle agglomeration occurred at high dosages, resulting in fewer catalyst active sites available for photon absorption to generate ·OH and $O_2^{\cdot -}$ radicals (Mohammadzadeh et al., 2015). In this

sense, it is noteworthy to operate photocatalytic treatment process below saturation level of Fe_2O_3-TiO_2 to reduce the expense of photocatalyst separation and light scattering effect (Hassan et al., 2016).

It was observed that the removal of COD was enhanced significantly with increasing air flow-rate but deteriorated at high flow-rate (Fig. 3b and c). Effect of air flow-rate was correlated to the amount of dissolved oxygen (DO) in the treatment system (Zangeneh et al., 2015). An increase of DO as electron scavengers was vital to trap photo-excited electron from the recombination in Fe_2O_3-TiO_2, hence, enhancing the photodegradation efficiency (Hassan et al., 2016). Furthermore, aeration via air bubbling provided sufficient energy to maintain good mixing of Fe_2O_3-TiO_2 particles in the suspension, in turn, promoting a higher mass transfer rate between contaminants and Fe_2O_3-TiO_2 (Zangeneh et al., 2015; Hassan et al., 2016). On the contrary, a decline in treatment efficiency at higher air flow-rate was attributed to an increase in bubbles volume fraction. Therefore, light penetration was hindered from reaching Fe_2O_3-TiO_2 to activate the photocatalyst sites (Zangeneh et al., 2015). In brief, optimum air flow-rate was an essential parameter in photocatalytic treatment.

An optimum photodegradation of 80.6% of COD removal was achieved using initial pH, photocatalyst dosage and air flow-rate of 3.88, 1.3 g/L and 2.28 L/min, respectively. The obtained experimental COD removal (80.6%) based on optimal conditions was very close to the predicted response (82.7%) from Eq. (3) with 2.5% error. Using RSM, the quadratic model and optimal treatment conditions could accurately represent the photocatalysis of PPME using Fe_2O_3-TiO_2.

3.3. Kinetics study on photodegradation of PPME using Fe_2O_3-TiO_2

Under optimized photocatalytic conditions, photodegradation of PPME using Fe_2O_3-TiO_2 fitted well with the Langmuir-Hinshelwood (L-H) kinetic model (Eq. (4)):

$$r = -\frac{dC}{dt} = \frac{kKC}{1 + KC_{initial}} \tag{4}$$

Where C is COD of PPME (mg/L) and $C_{initial}$ is initial COD of PPME (mg/L). K is L-H adsorption equilibrium constant, (L/mg) and it represents catalyst adsorption capacity. k is reaction rate constant (mg/L.min) and it is the proportionality constant for the intrinsic reactivity of photo-activated surface with C (Subramonian et al., 2014). The chosen L-H model was suitable to be applied for the current work because L-H model is commonly used to describe a plateau-type of kinetic profile, which concurred with the graphical plot in Fig. 2 (Subramonian et al., 2014). Furthermore, the present findings also agreed with the past studies that the established L-H model was the most appropriate kinetic model to describe photocatalysis using TiO_2-based catalyst and reactions involving photodegradation of organic pollutants (Luiz et al., 2015; He et al., 2016). Rate of photocatalytic activity was assumed to follow a first-order reaction (Eq. (5)):

$$r = -\frac{dC}{dt} = k_{app}C \tag{5}$$

where k_{app} (min^{-1}) is pseudo-first-order rate constant and it serves as a comparison and description for the photocatalytic reaction rate (Subramonian et al., 2014). Further integration of Eq. (5) yields Eqs. (6) and (7):

$$C = C_0 e^{-k_{app}t} \quad (6)$$

$$\ln C = -k_{app}t + \ln C_0 \quad (7)$$

Based on Eq. (7), k_{app} values were determined from gradients of straight line plots, ln C/C_0 against irradiation time (Fig. 4). Distinctly, reaction rate constant of Fe_2O_3-TiO_2 (9.2 x 10^{-3} min^{-1}) was 3.4-times greater than P25 (2.7 x 10^{-3} min^{-1}), validating that the synthesized Fe_2O_3-TiO_2 presented a far more superior photocatalytic ability than commercial P25. Suitability of L-H kinetic model to represent the photocatalytic reaction rate was further verified based on high R^2 values attained for both Fe_2O_3-TiO_2 and P25 plots (0.9872 and 0.9857 respectively).

3.4. Proposed reaction mechanism

Schematic diagram (Fig. 5) illustrates a possible photocatalytic reaction mechanism of Fe_2O_3-TiO_2 under UV irradiation (Ghorai et al., 2011; Moniz et al., 2014). To explain the distinct enhancement in photoactivity, the reaction mechanism relied on photo-generated electron-hole pairs in Fe_2O_3-TiO_2. Upon UV irradiation, electron-hole pairs were produced in conduction and valence bands of TiO_2 (Eq. (8)) (Hassan et al., 2016), forming a heterojunction between Fe_2O_3 and TiO_2 (Xia and Yin, 2013). Due to the difference between conduction bands of Fe_2O_3 and TiO_2 (2.2 and 3.2 eV, respectively), electrons generated in TiO_2 were easily transferred to the conduction band of Fe_2O_3 (Eq. (9)) (Ghorai et al., 2011; Moniz et al., 2014). The transferred electrons would then migrate to the surface of Fe_2O_3 to further assist in oxygen reduction to form $O_2^{\cdot -}$ during photocatalysis (Eq. (10)) (Ghorai et al., 2011). Meanwhile, vacant holes produced in the valence band of TiO_2 were transferred to the surface of TiO_2 for oxidation of water or surface

hydroxyl species into strong oxidizing ·OH radicals (Eq. (11)) (Subramonian et al., 2014; Hassan et al., 2016). The proposed reaction mechanism of Fe_2O_3-TiO_2 is represented by Eqs. (8-11):

$$TiO_2 + hv \rightarrow e_{CB}^{-} + h_{VB}^{+} \quad (8)$$

$$Fe^{3+} + e_{CB}^{-} \rightarrow Fe^{2+} \quad (9)$$

$$Fe^{2+} + O_2 \rightarrow Fe^{3+} + O_2^{\cdot -} \quad (10)$$

$$TiO_2\left(h_{VB}^{+}\right) + OH^{-}{}_{(ads)} \rightarrow TiO_2 + \cdot OH_{(ads)} \quad (11)$$

3.5. Effect of oxidants on treatment of PPME

Since the generation of ·OH radicals are of utmost importance in photocatalysis, effect of chemical oxidants (H_2O_2, BrO_3^-, and ClO^- ions) to produce more ·OH during treatment process were examined under optimal photocatalytic conditions. Photodegradation efficiency was further enhanced in the presence of H_2O_2, BrO_3^- or ClO^- (Fig. 6). As illustrated in Fig. 6a, an improvement in photocatalysis (80.6-84.8% of COD removal) due to H_2O_2 addition (0-0.500 mM) was attributed to additional generation of ·OH radicals and prevention of electron-hole pair recombination (Eqs. (12-14)) (Fathinia et al., 2015).

$$H_2O_2 + e_{CB}^{-} \rightarrow \cdot OH + OH^{-} \quad (12)$$

$$H_2O_2 + hv \rightarrow 2 \cdot OH \quad (13)$$

$$H_2O_2 + O_2^{\cdot -} \rightarrow \cdot OH + OH^- + O_2 \quad (14)$$

A drop in COD removal occurred at 0.625 mM because at higher H_2O_2 concentration, H_2O_2 acted as a scavenger for both ·OH and $O_2^{\cdot -}$, which resulted in a decrease in efficiency (Eqs. (15-17)) (Zangeneh et al., 2015).

$$H_2O_2 + \cdot OH \rightarrow HO_2 \cdot + H_2O \quad (15)$$

$$H_2O_2 + \cdot OH \rightarrow H_2O + O_2 \quad (16)$$

$$H_2O_2 + O_2 \cdot^- \rightarrow \cdot OH + OH^- + O_2 \quad (17)$$

BrO_3^- had been reported in the past of its ability to act as an effective electron acceptor, thus, the addition of BrO_3^- was of interest (Khodami et al., 2015). As portrayed in Fig. 6b, COD removal increased (80.6-85.8%) with increasing BrO_3^- concentration (0-2.5 mM). According to Eqs. (18) and (19), BrO_3^- was capable of inhibiting recombination of electron-hole pairs (Khodami et al., 2015). When the concentration of BrO_3^- was above 1.5 mM, the photodegradation efficiency did not significantly improve due to adsorption of excess Br^- on the surface of Fe_2O_3-TiO_2 (Chen and Liu, 2007).

$$BrO_3^- + 2H^+ + e_{CB}^- \rightarrow BrO_2 \cdot + H_2O \quad (18)$$

$$Br_3^- + 2H^+ + 6e_{CB}^- \rightarrow [BrO_2^-, HOBr] \rightarrow Br^- + 3H_2O \quad (19)$$

The use of ClO^- in treating PPME was investigated since it had been proven by a number of past studies that ClO^- had great capacity in oxidizing persistent organic toxins found in the wastewater (Fu et al., 2010). Noticeably, ClO^- (0-0.625 mM) proved to be the strongest oxidants among the tested additives with an astounding enhancement from 80.6 to 93.0% of COD removal (Fig. 6c). Enhancement in photodegradation was due to the formation of ·OH from direct photolysis of ClO^- ions (Eq. (20)) (Fu et al., 2010). Therefore, addition of ClO^- could be considered as a prospective photocatalytic enhancer in treating highly contaminated and recalcitrant wastewater.

$$HClO^- + hv \rightarrow Cl\cdot + O^- \rightarrow \cdot OH + Cl\cdot \quad (20)$$

3.6. Reusability and retrieval of Fe_2O_3-TiO_2

3.6.1. Stability and recyclability of reused Fe_2O_3-TiO_2

Recycling of Fe_2O_3-TiO_2 photocatalyst without significant loss in its photoactivity is crucial from economic and environmental standpoints for practical application (Das et al., 2014; Khodami et al., 2015). To ascertain the reusability of Fe_2O_3-TiO_2, the photocatalyst was reused for several cycles under optimal photocatalytic conditions. It was presented in Fig. 7 that there was a slight drop in photodegradation efficiency between the fresh and first-cycle of reused Fe_2O_3-TiO_2 (80.6 and 76.9% of COD removal, respectively). Despite that, the reused photocatalyst exhibited excellent chemical stability from the first to fifth cycles without significant decrease in photoactivity (76.9-75.6% of COD removal). Minor decline observed was due to poisoning of Fe_2O_3-TiO_2 active sites by adsorbed intermediates and pollutants, incomplete

recovery of Fe_2O_3-TiO_2, and possible separated phase of magnetic catalyst (Bai et al., 2016; Pang et al., 2016). Nonetheless, a minimal decrease in photocatalytic efficiency from the fresh to fifth-cycle of Fe_2O_3-TiO_2 (80.6-75.6% of COD removal) strongly supported that the mechanochemically synthesized Fe_2O_3-TiO_2 was stable and resistant towards photo-corrosion during photocatalytic reaction (Qin et al., 2014). The proven recyclability of Fe_2O_3-TiO_2 in this work served as a great advantage in reducing overall cost and minimizing environmental pollution (Bhosale et al., 2015).

3.6.2. Comparative characteristics of reused and fresh Fe_2O_3-TiO_2

Surface analysis revealed that the textural properties of mechanically milled Fe_2O_3-TiO_2 was higher than P25 (Table 4). The enhanced specific surface area and porosity provided a better surface adsorption and mass transfer between organic pollutants and Fe_2O_3-TiO_2 in the photocatalyst pores (Qin et al., 2014). This justified the improvement in photocatalytic activity of Fe_2O_3-TiO_2 as compared to P25. However, a slight detrimental in textural properties was noted from first to fifth cycles of reused Fe_2O_3-TiO_2 due to adsorption of impurities onto the photocatalyst (Wang et al., 2011).

FESEM images were taken to compare surface morphologies of fresh and reused Fe_2O_3-TiO_2, P25, and Fe_2O_3. Upon observation, there was no distinct change in morphologies between the fresh (Fig. 8a) and reused Fe_2O_3-TiO_2 (Fig. 8b). On the other hand, instead of uniformity in particle size as seen from P25 (inset in Fig. 8c), the fresh Fe_2O_3-TiO_2 was irregular in shape with slight agglomeration (Fig. 8a). However, Fe_2O_3-TiO_2 showed finer particles as compared to

Fe_2O_3 (Fig. 8d). The obtained surface morphology of Fe_2O_3-TiO_2 was induced by the effect of mechanical milling (Carneiro et al., 2014).

Based on Raman analysis (Fig. 9), characteristic peaks of reused Fe_2O_3-TiO_2 remained similar to the fresh Fe_2O_3-TiO_2, suggesting no new bonds were formed in the reused photocatalyst. Additionally, the attained Raman peaks were in fair agreement with literature review. Major Raman peaks detected at 155, 394, 514, and 633 cm^{-1} represented typical structure of TiO_2 whereas a peak at 205 cm^{-1} confirmed the presence of γ-Fe_2O_3 (Banisharif et al., 2015). Peak at 279 cm^{-1} was attributed to Fe-O-Ti bond in Fe_2O_3-TiO_2. This verified that Fe^{3+} replaced some of the Ti^{4+} species in TiO_2 lattice sites (Banisharif et al., 2015). Peak intensity corresponding to the presence of Fe_2O_3 was low due to low molar content of Fe_2O_3 (1 mol%) (Banisharif et al., 2015). An incorporation of Fe_2O_3 led to a shifting of peaks to slightly higher frequency due to the addition of Fe atoms into Ti lattice sites, which caused a distortion in the TiO_2 crystalline structure (Qin et al., 2014).

FTIR analysis was used to determine the functional groups present in the fresh and reused Fe_2O_3-TiO_2 (Fig. 10). As a comparison, FTIR spectra of both fresh and reused Fe_2O_3-TiO_2 were in close conformity. This indicated no new groups were formed in the reused photocatalyst despite five successive cycles, which concurred with Raman analysis (Fig. 9). FTIR spectrum of Fe_2O_3-TiO_2 was similar to P25, which denoted that Fe_2O_3 was well-infused into the TiO_2 lattice (Ghorai et al., 2011). Broad band at 3400 cm^{-1} was assigned to hydrogen bonded OH whereas band at 1634 cm^{-1} corresponded to the adsorbed water (Bai et al., 2016). These two bands played a significant role in photocatalytic reactions to react with photogenerated holes on Fe_2O_3-TiO_2 surface upon irradiation. Broad peak at 3250 cm^{-1} was ascribed to O-H stretching vibration (The

et al., 2015) while bands at 2924 and 2840 cm^{-1} were characteristics of C-H stretching vibrations from alkyl chain (Bhosale et al., 2015).

According to VSM analysis, an occurrence of small hysteresis loop at the magnetic hysteresis curves (M-H curves) (Fig. 11) for fresh and reused Fe_2O_3-TiO_2 indicated that both samples were ferromagnetic (Pang et al., 2016). Other magnetic properties of the samples are presented in Table 5. Saturation magnetization values (M_s) of the fresh and reused Fe_2O_3-TiO_2 were 5.23 and 1.95 emu/g, respectively. The M_s values were substantially lower than Fe_2O_3 (literature value = 58.56 emu/g) (Jayanthi et al., 2015). Drastic reduction in M_s values was attributed to the increase in specific surface area of the synthesized Fe_2O_3-TiO_2 (58.40 m^2/g) in comparison with bulk Fe_2O_3 (17.45 m^2/g) (Table 4) (Wang et al., 2011). Besides, TiO_2 is a non-ferromagnetic compound, thus, its coupling with Fe_2O_3 ultimately influenced the M_s value of Fe_2O_3-TiO_2 (Wang et al., 2011). On the other hand, the difference in M_s values between fresh and reused Fe_2O_3-TiO_2 could be due to the presence of post-treatment impurities adsorbed on the photocatalyst surface and trapped within the pores of the reused Fe_2O_3-TiO_2. This was verified by the reduction in pore volume and pore size of the reused Fe_2O_3-TiO_2 compared to the fresh Fe_2O_3-TiO_2 as shown in Table 4.

3.6.3. Potential retrieval of Fe_2O_3-TiO_2

Retrieval and separation of photocatalyst from an aqueous suspension remains as one of the most crucial issues in wastewater treatment. In this study, Fe_2O_3-TiO_2 was evaluated by its response towards a permanent magnet. As demonstrated in Fig. 12a, Fe_2O_3-TiO_2 photocatalyst was strongly attracted by the magnet, leaving a clear solution. This observation indicated a

promising and potential catalyst recovery method using an applied external magnetic field. Moreover, desirably low remnant magnetization values of Fe_2O_3-TiO_2 (Table 5) evidenced that the retrieved Fe_2O_3-TiO_2 could be easily re-dispersed into the aqueous suspension for reuse purpose (Pang et al., 2016).

Other than employing an external magnetic field for photocatalyst recovery, Fig. 12b and c demonstrated the possibility of retrieving Fe_2O_3-TiO_2 photocatalyst through sedimentation. Owing to its higher porosity (Table 4) (Qin et al., 2014), Fe_2O_3-TiO_2 was easily and well separated by sedimentation from the suspension within 1 h whereas suspension containing P25 remained turbid. These observations supported an alternative Fe_2O_3-TiO_2 recovery method via sedimentation, which was particularly favourable for long-operation photocatalysis at an industrial scale (Qin et al., 2014). Overall, the magnetic responsiveness and effective sedimentation elucidated that the synthesized Fe_2O_3-TiO_2 could be readily retrieved and recycled.

3.7. Other characteristics of Fe_2O_3-TiO_2

3.7.1. Thermal properties

Thermal stability of Fe_2O_3-TiO_2 was represented by the displayed TG curve (Fig. 13). Weight loss occurred at 105 °C was due to the removal of adsorbed water (Patra et al. 2012; Bhosale et al., 2015). A minimal weight loss of 2.2% confirmed that Fe_2O_3-TiO_2 was completely dehydrated rather than decarbonized (Wu et al., 2015). This denoted the dual existence of Fe_2O_3 and TiO_2 in Fe_2O_3-TiO_2 without addition of other carbonaceous materials during mechanochemical synthesis.

3.7.2. Electrokinetic behaviour

Zeta potential analysis was conducted to measure surface charge and electrophoretic mobility of Fe_2O_3-TiO_2 in the aqueous suspension (Pang et al., 2016). Fig. 14 shows that the zeta potential values of Fe_2O_3-TiO_2 decreased from 36.0 to -38.9 mV with increasing pH (pH 2 to 10). Similar trend was observed for P25. Change in surface charge was dependent on adsorbed hydroxyl groups on the photocatalyst surface. At alkaline conditions, Fe_2O_3-TiO_2 was more negatively charged and showed negative zeta potential values due to the formation of $Fe\text{-}O^-$ and $Ti\text{-}O^-$ (Pang et al., 2016). Conversely, charge on Fe_2O_3-TiO_2 surface was positive due to $Fe\text{-}OH_2^+$ and $Ti\text{-}OH_2^+$ formation at acidic conditions (Pang et al., 2016). Existence of these surface hydroxyl groups played a crucial role in photocatalytic reactions by reacting with the photogenerated holes to produce ·OH (Pang et al., 2016). Isoelectric point or point of zero charge (pzc) is the point at which the surface charge becomes neutral at a certain pH. Hence, for suspension with $pH < pH_{pzc}$, the photocatalyst surface is positively charged and at $pH > pH_{pzc}$, it is negatively charged (Pang et al., 2016). The pH_{pzc} of Fe_2O_3-TiO_2 and P25 were at pH 5.8 and 5.5, respectively. The slight deviation in pH_{pzc} was due to replacement of Ti^{4+} by Fe^{3+} species in TiO_2 lattice of Fe_2O_3-TiO_2 (Carneiro et al., 2014).

4. Conclusion

In summary, real PPME was effectively degraded via heterogeneous photocatalysis using a magnetically retrievable Fe_2O_3-TiO_2 photocatalyst. A solvent-free and simple mechanochemical process via ball milling was chosen to fabricate Fe_2O_3-TiO_2 as an initiative towards green

chemistry. Characterization study revealed that the synthesized Fe_2O_3-TiO_2 had high ferromagnetism and enhanced catalyst properties in terms of specific surface area (58.40 m^2/g), porosity (pore volume and pore size of 0.29 cm^3/g and 18.52 nm, respectively), and band gap (2.95 eV). In addition, reusability study proved that Fe_2O_3-TiO_2 was chemically stable and resistant towards photo-corrosion up to five successive cycles without significant change in its photoactivity and intrinsic properties. Moreover, Fe_2O_3-TiO_2 exhibited potential retrieval from aqueous suspension by using an applied magnetic field or sedimentation. Using RSM, the optimal conditions were initial effluent pH = 3.88, [Fe_2O_3-TiO_2] = 1.3 g/L, and air flow-rate = 2.28 L/min. These conditions enabled 80.6% removal of COD from the PPME using Fe_2O_3-TiO_2 and the COD removal was approximately 2-times greater than using P25. It was also found that photocatalysis of PPME using Fe_2O_3-TiO_2 was well-fitted to the L-H kinetic model with an apparent rate constant (9.2×10^{-3} min^{-1}) 3.4-times greater than P25 (2.7×10^{-3} min^{-1}). Additionally, the presence of reactive oxidants (H_2O_2, BrO_3^-, and ClO^- ions) enhanced the treatment efficiency considerably from 80.6 to 93.0% of COD removal with 0.625 mM of ClO^-. Evidently, the present study proved that the magnetic Fe_2O_3-TiO_2 was able to degrade real industrial wastewater with promising retrieval and reuse potentials.

Acknowledgements

The authors would like to thank Monash University Malaysia for providing W. Subramonian with a PhD scholarship.

References

Ashrafi, O., Yerushalmi, L., Haghighat, F., 2015. Wastewater treatment in the pulp-and-paper industry: a review of treatment processes and the associated greenhouse gas emission. J. Environ. Manage. 158, 146-157.

Bai, Z.Y., Yang, Q., Wang, J.L., 2016. Fe_3O_4/multi-walled carbon nanotubes as an efficient catalyst for catalyst for catalytic ozonation of p-hydroxybenzoic acid. Int. J. Environ. Sci. Technol. 13, 483-492.

Banisharif, A., Khodadadi, A.A., Mortszavi, Y., Firooz, A.A., Behestian, J., Agah, S., Menbari, S., 2015. Highly active Fe_2O_3-doped TiO_2 photocatalyst for degradation of trichloroethylene in air under UV and visible light irradiation: experimental and computational studies. Appl. Catal. B-Environ. 165, 209-221.

Bhanarkar, A.D., Gupta, R.K., Biniwale, R.B., Tamhane, S.M., 2014. Nitric oxide absorption by hydrogen peroxide in airlift reactor: A study using response surface methodology. Int. J. Environ. Sci. Technol. 11, 1537-1548.

Bhattacharjee, S., Chakraborty, S., Mandol, K., Liu, L., Choi, H., Bhattacharjee, C., 2015. Optimization of process parameters during photocatalytic degradation of phenol in UV annular reactor. Desalin. Water Treat. 54, 2270-2279.

Bhosale, M.A., Ummineni, D., Sasaki, T., Nishio-Hamane, D., Bhanage, B.M., 2015. Magnetically separable γ-Fe_2O_3 nanoparticles: an efficient catalyst for acrylation of

alcohols, phenols, and amines using sonication energy under solvent free condition. J. Mol. Catal. A-Chem. 404-405, 8-17.

Brzozowski, B., Lewandowska, M., 2014. Prolyl endopeptidase-optimization of medium and culture conditions for enhanced production by *Lactobacillus acidophilus*. Electron. J. Biootechnol. 17, 204-210.

Cao, M., Wang, P., Ao, Y., Wang, C., Hou, J., Qian, J., 2015. Photocatalytic degradation of tetreabromobisphenol A by magnetically separable graphene-TiO_2 composite photocatalyst: mechanism and intermediate analysis. Chem. Eng. J. 264, 113-124.

Carneiro, J.O., Azevedo, S., Fernandes, F., Freitas, E., Pereira, M., Tavares, C.J., Lanceros-Méndez, S., Teixeira, V., 2014. Synthesis of iron-doped TiO_2 nanoparticles by ball-milling process: the influence of process parameters on the structural, optical, magnetic, and photocatalytic properties. J. Mater. Sci. 49, 7476-7488.

Chen, S., Liu, Y., 2007. Study on the photocatalytic degradation of glyphosate by TiO_2 photocatalyst. Chemosphere 67, 1010-1017.

Chin, H.N., Noor, Z.Z., Mutamin, N.S.A., Chi, K.L., 2016. Green Technology in wastewater treatment technologies: integration of membrane bioreactor with various wastewater treatment systems. Chem. Eng. J. 283, 582-594.

Das, R., Sarkar, S., Chakraborty, S., Choi, H., Bhattacharjee, C., 2014. Remediation of antiseptic components in wastewater by photocatalysis using TiO_2 nanoparticles. Ind. Eng. Chem. Res. 53, 3012-3020.

Debnath, S., Ballav, N., Nyoni, H., Maity, A., Pillay, K., 2015. Optimization and mechanism elucidation of the catalytic photo-degradation of the dyes Eosin Yellow (EY) and Naphthol blue black (NBB) by a polyaniline-coated titanium dioxide nanocomposite. Appl. Catal. B-Environ. 1653, 330-342.

Fathinia, S., Fathinia, M., Rahmani, A.A., Khataee, A., 2015. Preparation of natural pyrite nanoparticles by high energy planetary ball milling as a nanocatalyst for heterogeneous Fenton process. Appl. Surf. Sci. 327, 190-200.

Fu, J., Xu, Z., Li, Q.-S., Chen, S., An, S.-Q., Zeng, Q.-F., Zhu, H.-L., 2010. Treatment of simulated wastewater containing Reactive Red 195 by zero-valent iron/ activated carbon combined with microwave discharge electrodeless lamp/ sodium hypochlorite. J. Environ. Sci. 22, 512-518.

Ghorai, T.K., Chakraborty, M., Pramanik, P., 2011. Photocatalytic performance of nano-photocatalyst from TiO_2 and Fe_2O_3 by mechanochemical synthesis. J. Alloy. Compd. 509, 8158-8164.

Gimeno, O., García-Araya, J.F., Rivas, F.J., Espejo, A., 2016. Removal of emerging contaminants from a primary effluent of municipal wastewater by means of sequential

biological degradation-solar photocatalytic oxidation processes. Chem. Eng. J. 290, 12-20.

Hassan, M., Zhao, Y., Xie, B., 2016. Employing TiO_2 photocatalysis to deal with landfill leachate: current status and development. Chem. Eng. J. 285, 264-275.

Hay, J.X.W., Wu, T.Y., Juan, J.C., Jahim, J.M., 2015. Improved biohydrogen production and treatment of pulp and paper mill effluent through ultrasonication pretreatment of wastewater. Energ. Convers. Manage. 106, 576-583.

Hay, J.X.W., Wu, T.Y., Ng, B.J., Juan, J.C., Jahim, J.M., 2016. Reusing pulp and paper mill effluent as a bioresource to produce biohydrogen through ultrasonicated *Rhodobacter sphaeroides*. Energ. Convers. Manage. 113, 273-280.

Hay, J.X.W., Wu, T.Y., Teh, C.Y., Jahim J.Md., 2012. Optimized growth of Rhodobacter sphaeroides O.U.001 using response surface methodology (RSM). J. Sci. Ind. Res. 71, 149-154.

He, Y., Sutton, N.B., Rijnaarts, H.H.H., Langenhoff, A.A.M., 2016. Degradation of pharmaceuticals in wastewater using immobilized TiO_2 photocatalysis under simulated solar irradiation. Appl. Catal. B-Environ. 182, 132-141.

Hermosilla, D., Merayo, N., Gascó, A., Blanco, Á., 2015. The application of advanced oxidation technologies to the treatment of effluents from pulp and paper industry: a review. Environ. Sci. Pollut. Res. 22, 168-191.

Jayanthi, S.A., Nathan, D.M.G.T., Jayashainy, J., Sagayaraj, P., 2015. A novel hydrothermal approach for synthesizing α-Fe_2O_3, γ-Fe_2O_3 and Fe_3O_4 mesoporous magnetic nanoparticles. Mater. Chem. Phys. 162, 316-325.

Kamali, M., Khodaparast, Z., 2015. Review on recent developments on pulp and paper mill wastewater treatment. Ecotox. Environ. Safe. 114, 326-342.

Khodami, Z., Nezamzadeh-Ejhieh, A., 2015. Invesitgation of photocatalytic effect of ZnO-SnO_2 /nano clinoptilolite system in the photodegradation of aqueous mixture of 4-methylbenzoic acid/ 2-chloro-5-nitrobenzoic acid. J. Mol. Catal. A-Chem. 409, 59-68.

Low, F.C.F., Wu, T.Y., Teh, C.Y., Juan, J.C., Balasubramanian, N., 2012. Investigation into photocatalytic decolorisation of CI Reactive Black 5 using titanium dioxide nanopowder. Color. Technol. 128, 44-50.

Luiz, D.d.B., José, H.J., Moreira, R.d.F.P.M., 2015. Kinetics of photocatalytic reduction of nitrate in synthetic and real effluent using TiO_2 doped with Zn as photocatalyst. J. Chem. Biotechnol. 90, 821-829.

MIDA, 2015. Malaysia investment performance report 2015: driving sustainable growth, Malaysian Investment Development Authority.

Mohammadzadeh, S., Olya, A.M., Shariati, A., Nikou, K.M.R., 2015. Synthesis, characterization and application of ZnO-Ag as a nanophotocatalyst for organic compounds degradation, mechanism and economic study. J. Environ. Sci. 35, 194-207.

Moniz, S.J.A., Shevlin, S.A., An, X., Guo, Z.-X., Tang, J., 2014. Fe_2O_3-TiO_2 nanocomposites for enhanced charge separation and photocatalytic activity. Chem. Eur. J. 20, 15571-15579.

Naik, S.S., Setty, Y.P., 2014. Optimization of parameters using response surface methodology and genetic algorithm for biological denitrification of wastewater. Int. J. Environ. Sci. Technol. 11, 1537-1548.

Pang, Y.L., Lim, S., Ong, H.C., Chong, W.T., 2016. Synthesis, characteristics and sonocatalytic activities of calcined γ-Fe_2O_3 and TiO_2 nanotubes/ γ-Fe_2O_3 magnetic catalyst in the degradation of Orange G. Ultrason. Sonochem. 29, 317-327.

Patra, A.K., Dutta, A., Bhaumik, A., 2012. Highly ordered mesoporous TiO_2-Fe_2O_3 mixed oxide synthesized by sol-gel pathway: an efficient and reusable heterogeneous catalyst for dehalonegation reaction. ACS Appl. Mater. Interfaces 4, 5022-5028.

Qin, L., Pan, X., Wang, L., Sun, X., Zhang, G., Guo, X., 2014. Facile preparation of mesoporous TiO_2 (B) nanowires with well-dispersed Fe_2O_3 nanoparticles and their photochemical catalytic behavior. Appl. Catal. B-Environ. 150-151, 544-553.

Shak, K.P.Y., Wu, T.Y., 2015. Optimized use of alum together with unmodified *Cassia obtusifolia* seed gum as a coagulant aid in treatment of palm oil mill effluent under natural pH of wastewater. Ind. Crops Prod. 76, 1169-1178.

Soleymani, F., Khani, M.H., Pahlavanzadeh, H., Manteghian, M., 2015. Study of cobalt (II) biosorption on *Sargassum* sp. by experimental design methodology. Int. J. Environ. Sci. Technol. 12, 1907-1922.

Sridhar, R., Sivakumar, V., Prakash Maran, J., Thirugnanasambandham, K., 2104. Influence of operating parameters on treatment of egg processing effluent by electrocoagulation process. Int. J. Sci. Technol. 11, 1619-1630.

Subramonian, W., Wu, T.Y., 2014. Effect of enhancers and inhibitors on photocatalytic sunlight treatment of methylene blue. Water Air Soil Pollut. 225, 1-15.

Subramonian, W., Wu, T.Y., Chai, S.-P., 2014. A comprehensive study on coagulant performance and floc characterization of natural *Cassia obtusifolia* seed gum in treatment of raw pulp and paper mill effluent. Ind. Crops Prod. 61, 317-324.

Subramonian, W., Wu, T.Y., Chai, S.-P., 2015. An application of response surface methodology for optimizing coagulation process of raw industrial effluent using *Cassia obtusifolia* seed gum together with alum. Ind. Crops Prod. 70, 107-115.

Teh, C.Y., Budiman, P.M., Shak, K.P.Y., Wu, T.Y., 2016. Recent advancement of coagulation-flocculation and its application in wastewater treatment. Ind. Eng. Chem. Res. 55, 4363-4389.

Teh, C.Y., Wu, T.Y., Juan, J.C., 2014. Optimization of agro-industrial wastewater treatment using unmodified rice starch as a natural coagulant. Ind. Crops Prod. 56, 17-26.

Teh, C.Y., Wu, T.Y., Juan, J.C., 2015. Facile sonochemical synthesis of N,Cl-codoped TiO_2: synthesis effects, mechanism and photocatalytic performance. Catal. Today 256, 365-374.

Visa, M., Andronic, L., Duta, A., 2015. Fly ash-TiO_2 nanocomposite material for multi-pollutants wastewater treatment. J. Environ. Manage. 150, 336-343.

Wang, H., Fei, X., Wang, L., Li, Y., Xu, S., Sun, M., Sun, L., Zhang, C., Li, Y., Yang, Q., Wei, Y., 2011. Magnetically separable iron oxide nanostructures-TiO_2 nanofibers hierarchical heterostructures: controlled fabrication and photocatalytic activity. New J. Chem. 35, 1795-1802.

Wang, Y., Fan, X., Wang, S., Zhang, G., Zhang, F., 2013. Magnetically separable γ-Fe_2O_3/TiO_2 nanotubes for photodegradation of aqueous methyl orange. Mater. Res. Bull. 48, 785-789.

World Bank Group, 2007. Environmental, health, and safety guidelines pulp and paper mils. International Finance Corporation.

Wu, G., Cheng, Y., Ren, Y., Wang, Y., Wang, Z., Wu, H., 2015. Synthesis and characterization of γ-Fe_2O_3@C nanorod-carbon sphere composite and its application as microwave absorbing material. J. Alloy. Compd. 652, 346-350.

Wu, T.Y., Mohammad, A.W., Jahim, J. Md.. Anuar, N., 2009. Optimized reuse and bioconversion from retentate of pre-filtered palm oil mill effluent (POME) into

microbial protease by Aspergillus terreus using response surface methodology. J. Chem. Technol. Biotechnol. 84, 1390-1396.

Xia, Y., Yin, L., 2013. Core-shell structured α-Fe_2O_3@TiO_2 nanocomposited with improved photocatalytic activity in the visible light region. Phys. Chem. Chem. Phys. 15, 18627-186634.

Yao, H., Fan, M., Wang, Y., Luo, G., Fei, W., 2015. Magnetic titanium dioxide based nanomaterials: synthesis, characteristics, and photocatalytic application in pollutant degradation. J. Mater. Chem. A 3, 17511-17524.

Zangeneh, H., Zinatizadeh, A.A.L., Habibi, M., Akia, M., Isa, M.H., 2015. Photocatalytic oxidation of organic dyes and pollutants in wastewater using different modified titanium dioxides: a comparative review. J. Ind. Eng. Chem. 26, 1-36.

Zhong, J., Zhang, X., Ren, Y., Yang, J., Tan, H., Zhou, J., 2014. Optimization of *Bacillus subtilis* cell growth effecting jiean-peptide production in fed batch fermentation using central composite design. Electron. J. Biotechnol. 17, 132-136.

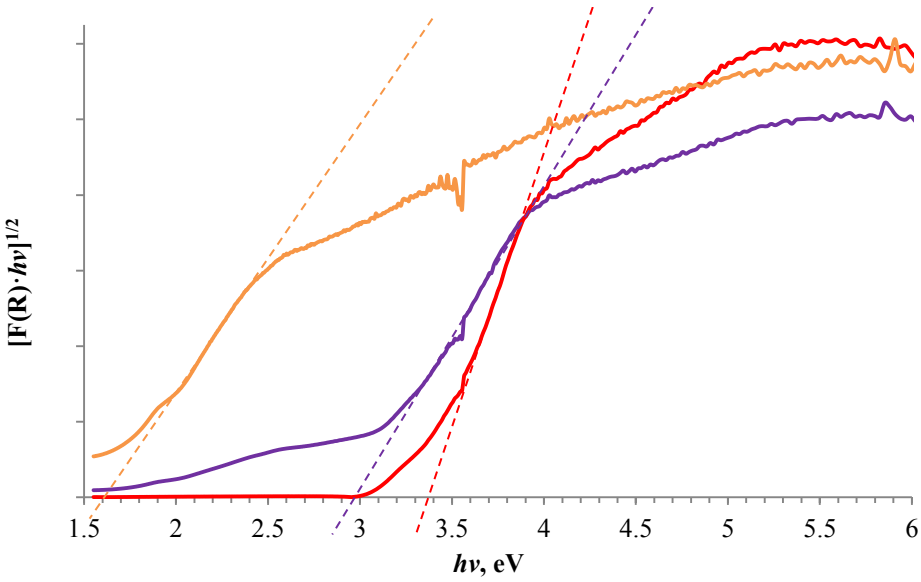

Fig. 1. Plot of transformed Kulbeka-Munk function $[F(R)\cdot h\nu]^{1/2}$ versus $h\nu$ of Fe_2O_3-TiO_2 (purple), P25 (red), and Fe_2O_3 (brown).

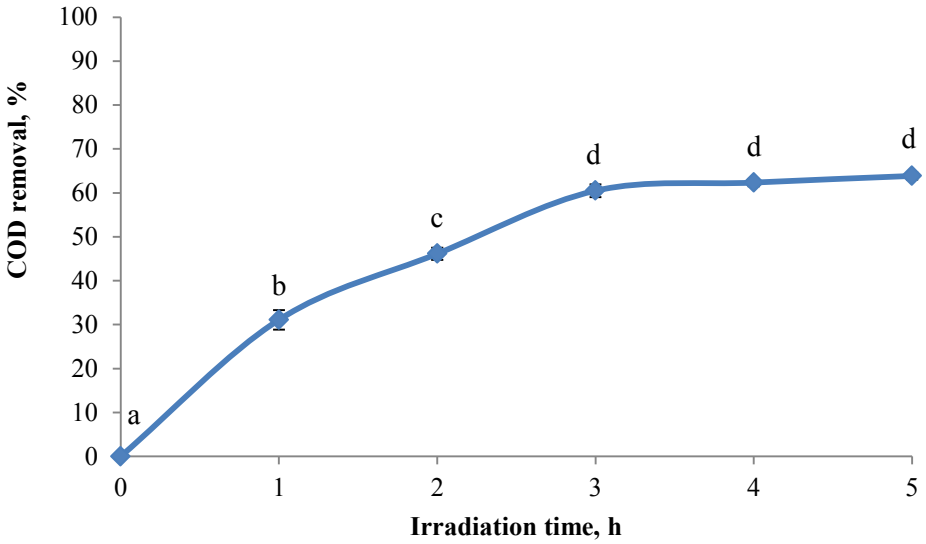

Fig. 2. Effect of irradiation time on photodegradation of PPME. (milling time = 20 min; milling speed = 250 rpm; $[Fe_2O_3]$ = 1 mol%; ball:powder mass ratio = 10:1; initial pH = 4; $[Fe_2O_3$-$TiO_2]$ = 1.0 g/L; air flow-rate = 4.0 L/min; n = 3). Values annotated with different letters represent significant differences (one-way ANOVA, Tukey's test; $P < 0.05$).

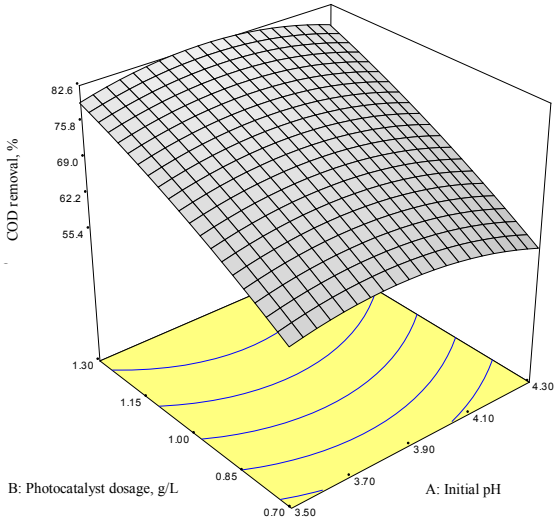
82.6
75.8
69.0
62.2
55.4
COD removal, %
1.30
1.15
1.00
0.85
0.70
B: Photocatalyst dosage, g/L
3.50
3.70
3.90
4.10
4.30
A: Initial pH

Fig. 3. (a)

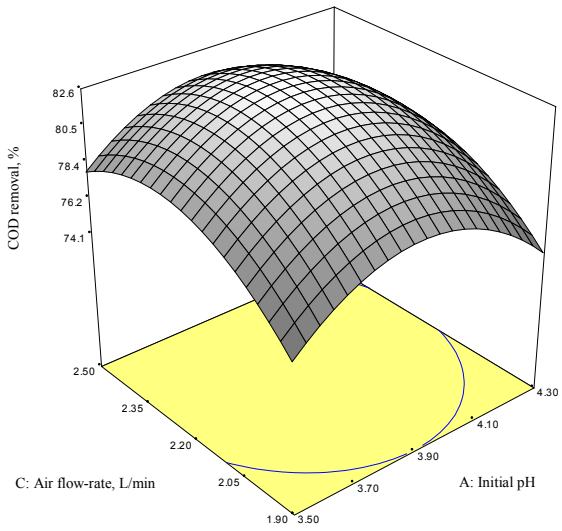
82.6
80.5
78.4
76.2
74.1
COD removal, %
2.50
2.35
2.20
2.05
1.90
C: Air flow-rate, L/min
3.50
3.70
3.90
4.10
4.30
A: Initial pH

Fig. 3. (b)

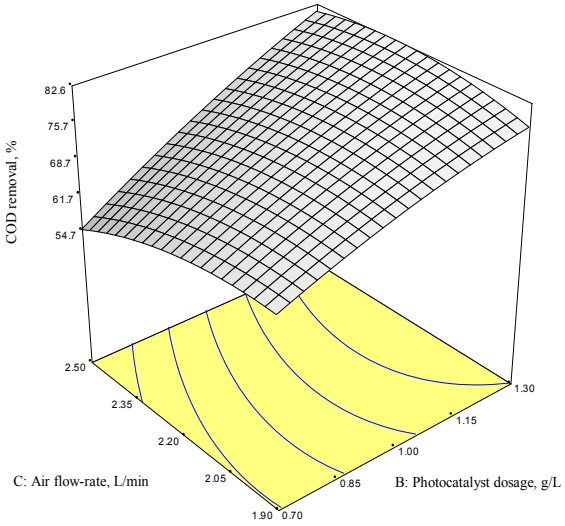

Fig. 3. (c)

Fig. 3. 3-D response surface plots of COD removal from PPME as a function of (a) initial pH and Fe_2O_3-TiO_2 dosage, (b) initial pH and air flow-rate, and (c) Fe_2O_3-TiO_2 dosage and air flow-rate.

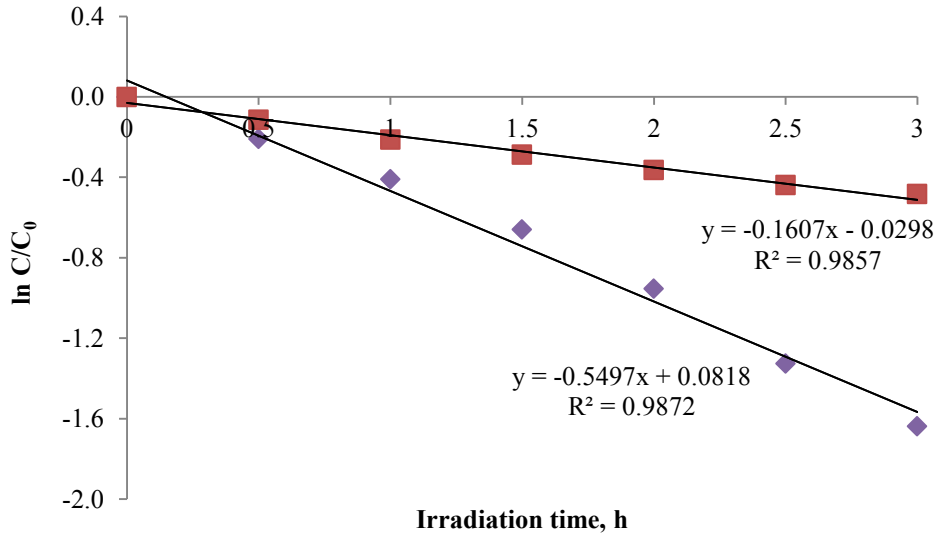

Fig. 4. Kinetic study on photodegradation of PPME under optimal conditions (initial pH = 3.88, [Fe_2O_3-TiO_2] = 1.3 g/L, and air flow-rate = 2.28 L/min).

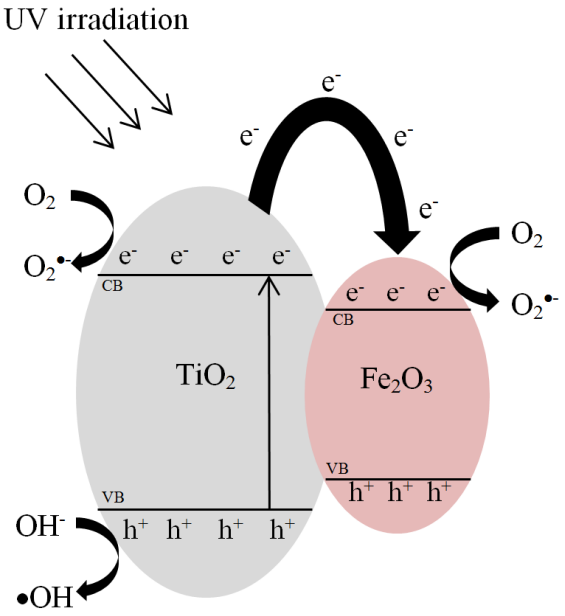

Fig. 5. Proposed photocatalytic mechanism of Fe_2O_3-TiO_2.

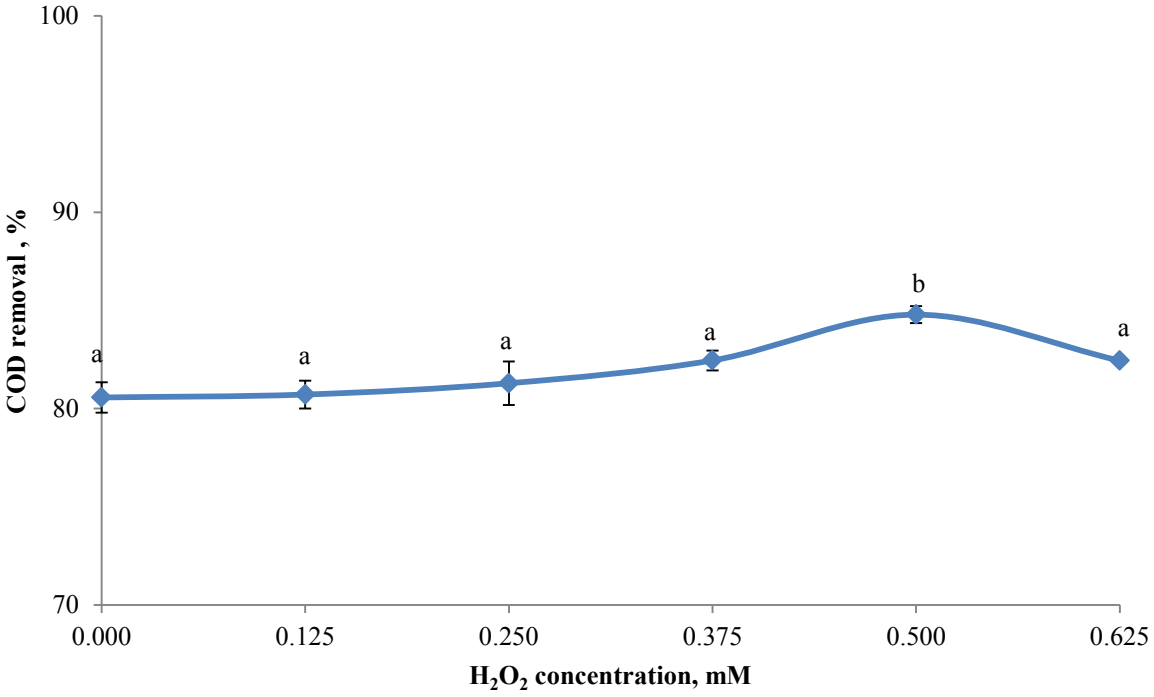

Fig. 6. (a)

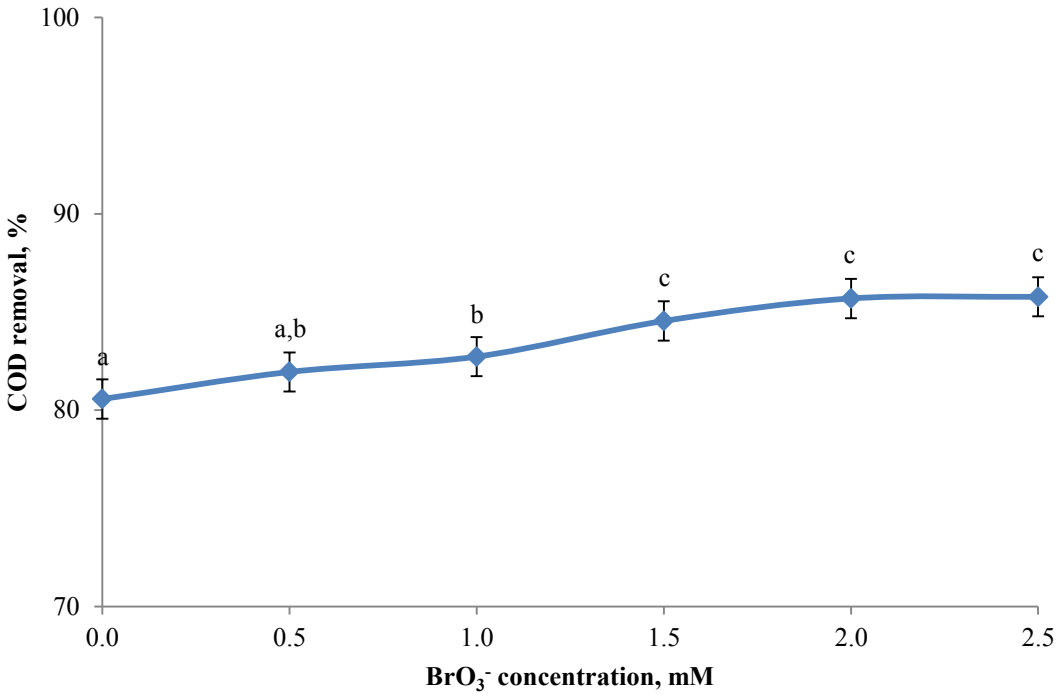
100
90
80
70
COD removal, %
a
a,b
b
c
c
c
0.0
0.5
1.0
1.5
2.0
2.5
BrO3- concentration, mM

Fig. 6. (b)

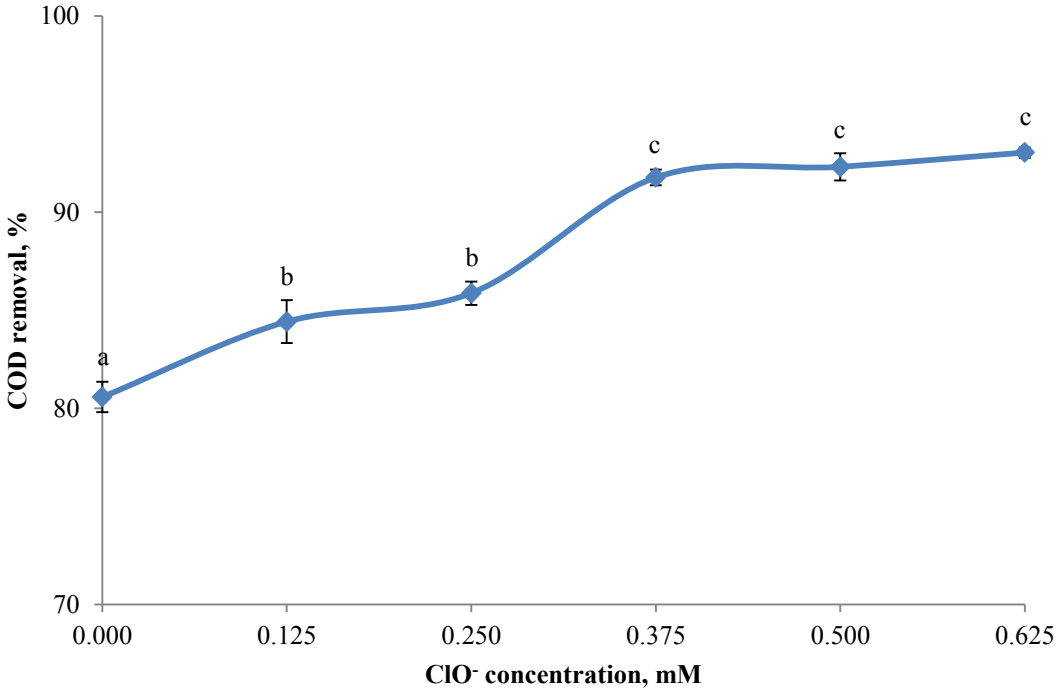
100
90
80
70
COD removal, %
a
b
b
c
c
c
0.000
0.125
0.250
0.375
0.500
0.625
ClO- concentration, mM

Fig. 6. (c)

Fig. 6. Effect of (a) H_2O_2 (b) BrO_3^-, and (c) ClO^- addition on photodegradation of PPME under optimal conditions (initial pH = 3.88, [Fe_2O_3-TiO_2] = 1.3 g/L, and air flow-rate = 2.28 L/min). Photodegradation of PPME using 0.5 mM H_2O_2, 1.5 mM BrO_3^-, or 0.375 mM ClO^- in the absence of photocatalyst under optimal conditions resulted in 2.8, 3.6 and 9.7% COD removals, respectively.

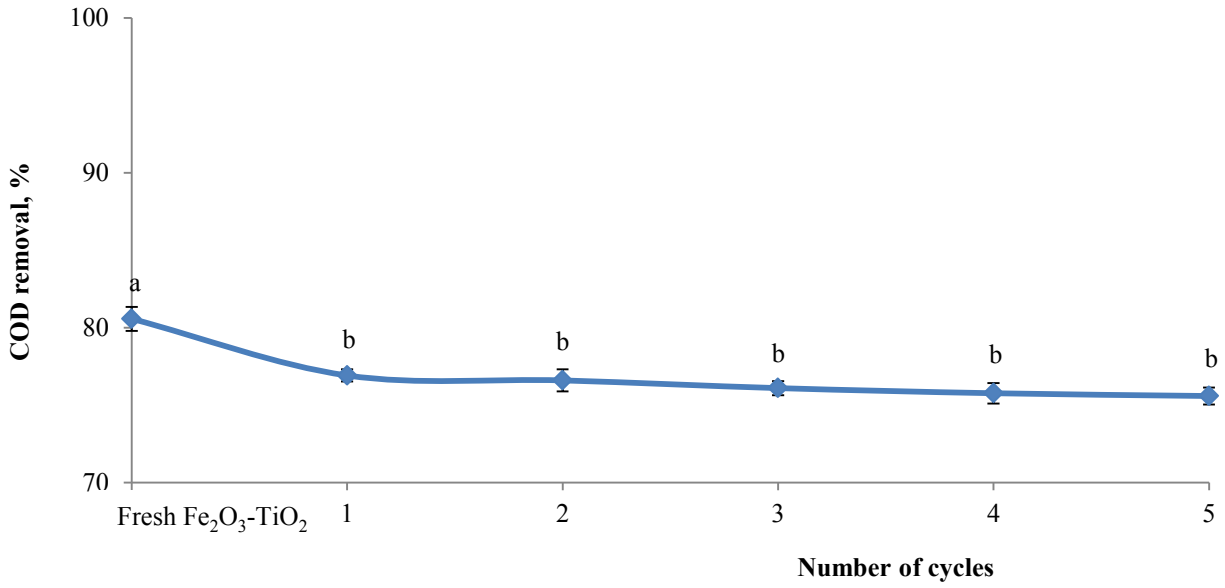

Fig. 7. Reusability of Fe_2O_3-TiO_2 in photodegradation of PPME under optimal conditions (initial pH = 3.88, [Fe_2O_3-TiO_2] = 1.3 g/L, and air flow-rate = 2.28 L/min).

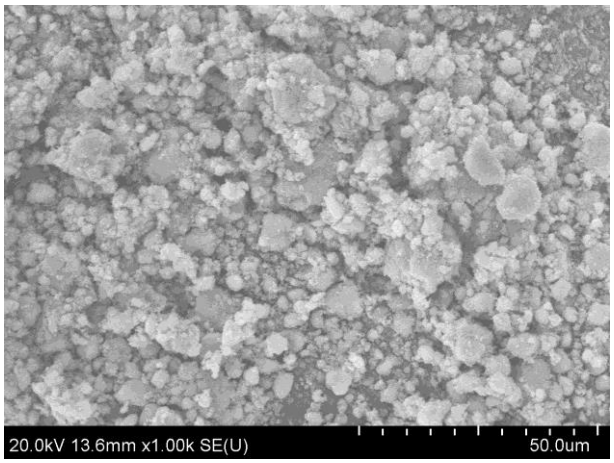

Fig. 8. (a)

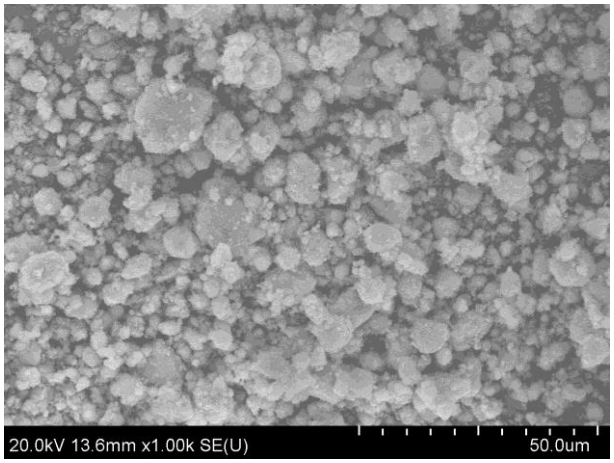

Fig. 8. (b)

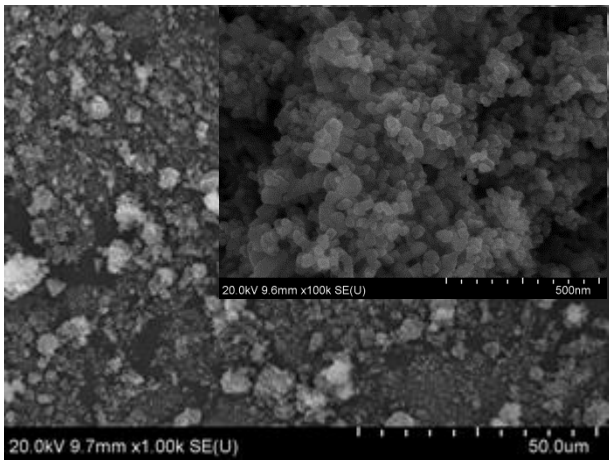

Fig. 8. (c)

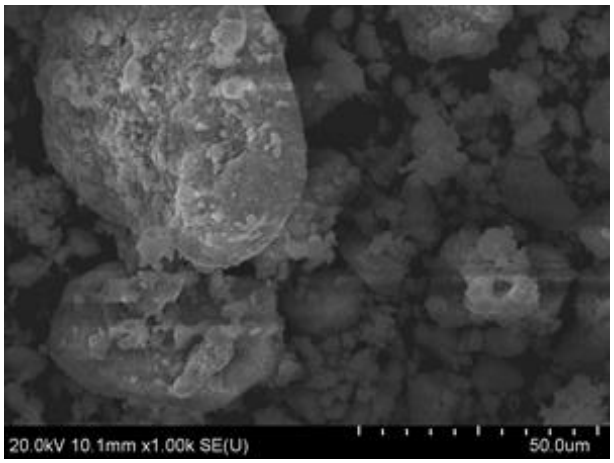

Fig. 8. (d)

Fig. 8. FESEM images of (a) fresh Fe_2O_3-TiO_2, (b) reused Fe_2O_3-TiO_2, (c) P25, and (d) Fe_2O_3.

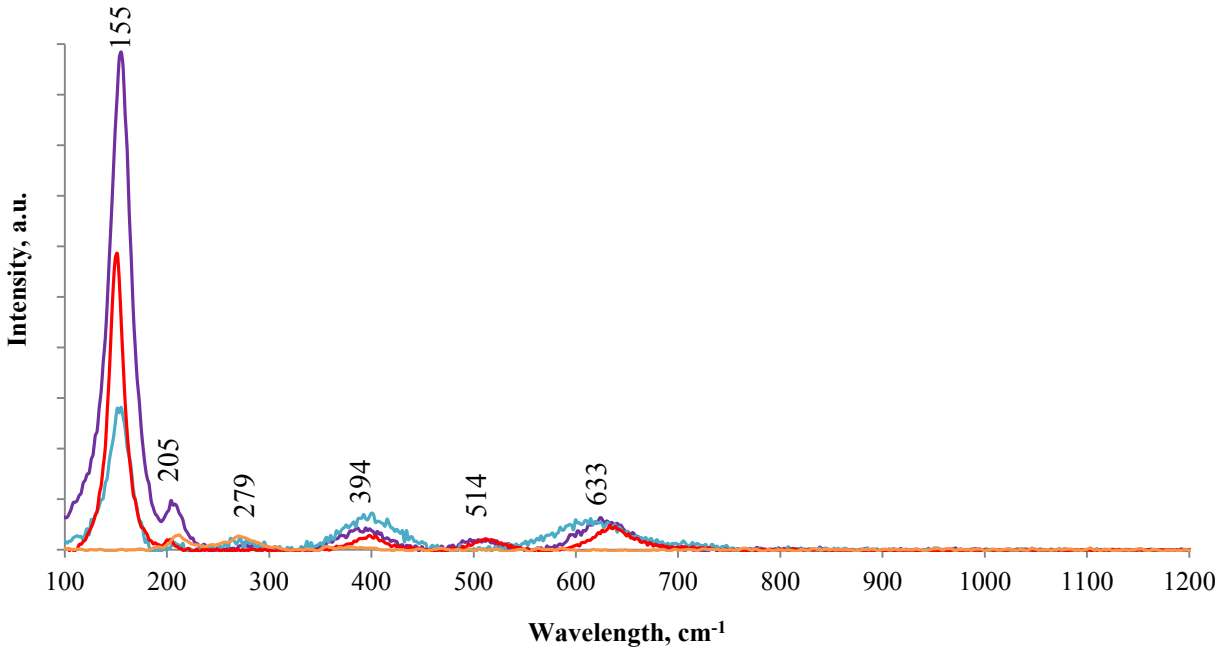

Fig. 9. Raman spectra of fresh Fe_2O_3-TiO_2 (purple), reused Fe_2O_3-TiO_2 (blue), P25 (red), and Fe_2O_3 (brown).

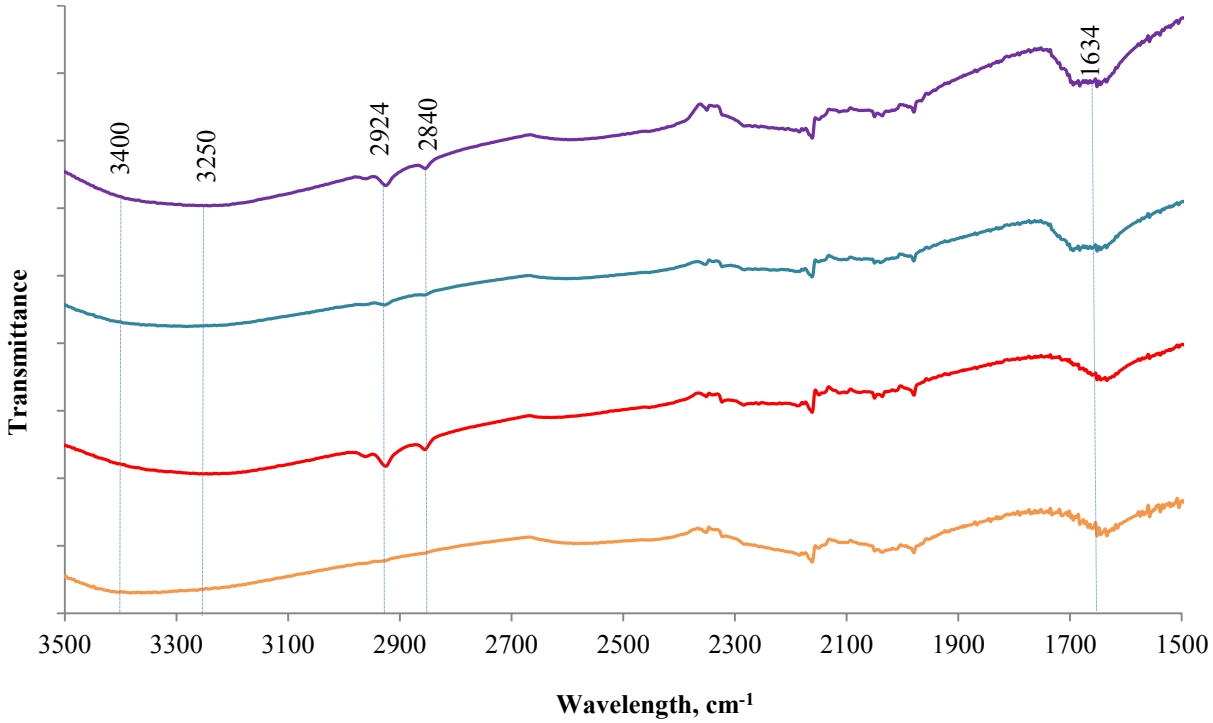

Fig. 10. FTIR spectra of fresh Fe_2O_3-TiO_2 (purple), reused Fe_2O_3-TiO_2 (blue), P25 (red), and Fe_2O_3 (brown).

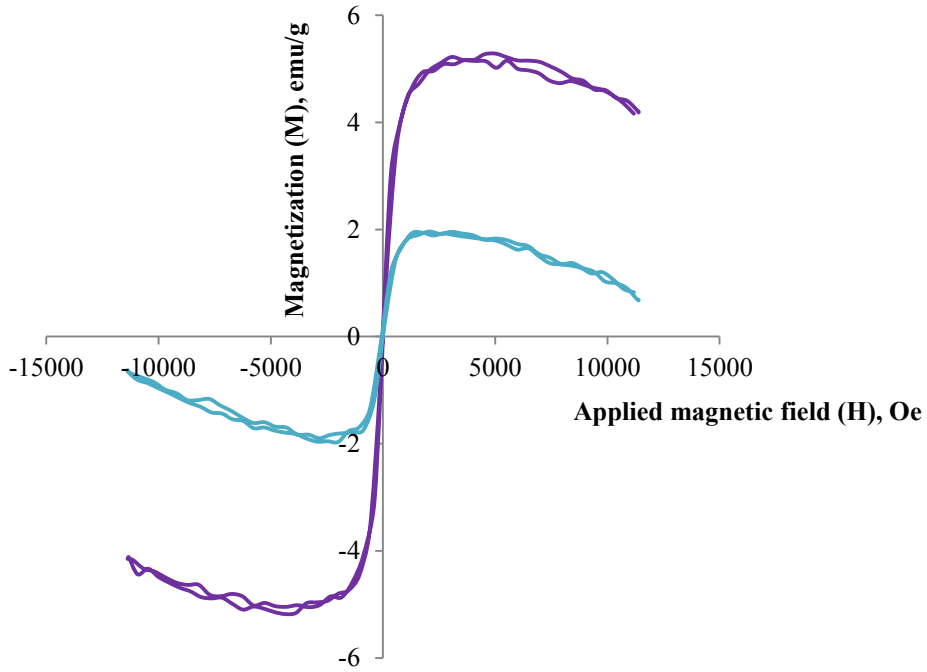

Fig. 11. M-H curves of fresh Fe_2O_3-TiO_2 (purple) and reused Fe_2O_3-TiO_2 (blue).

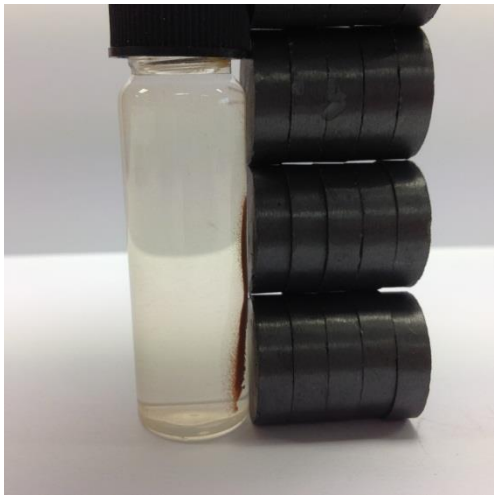

Fig. 12. (a)

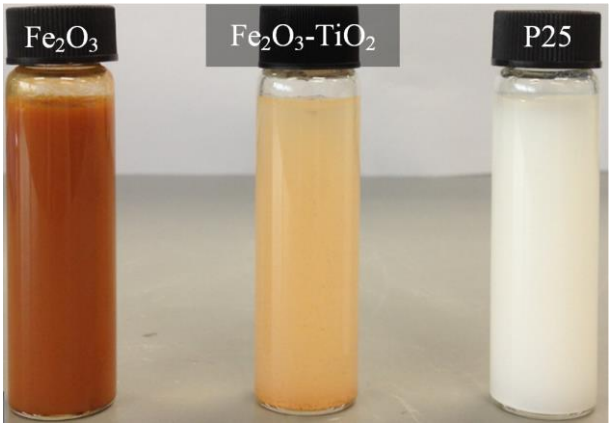

Fig. 12. (b)

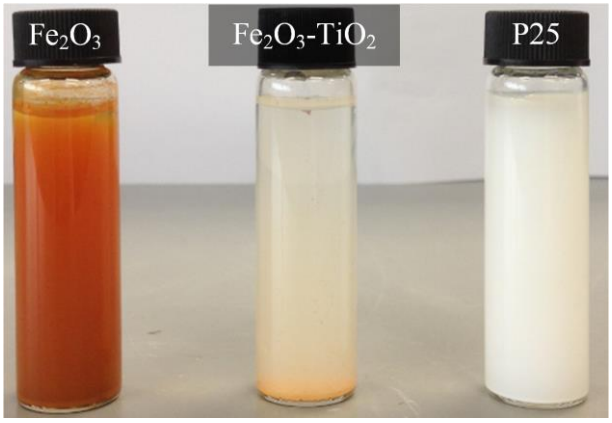

Fig. 12. (c)

Fig. 12. (a) Magnetic separation of Fe_2O_3-TiO_2 from aqueous suspension. Sedimentation of Fe_2O_3, Fe_2O_3-TiO_2, and P25 in aqueous suspension for (b) 0 min and (c) 1 hour.

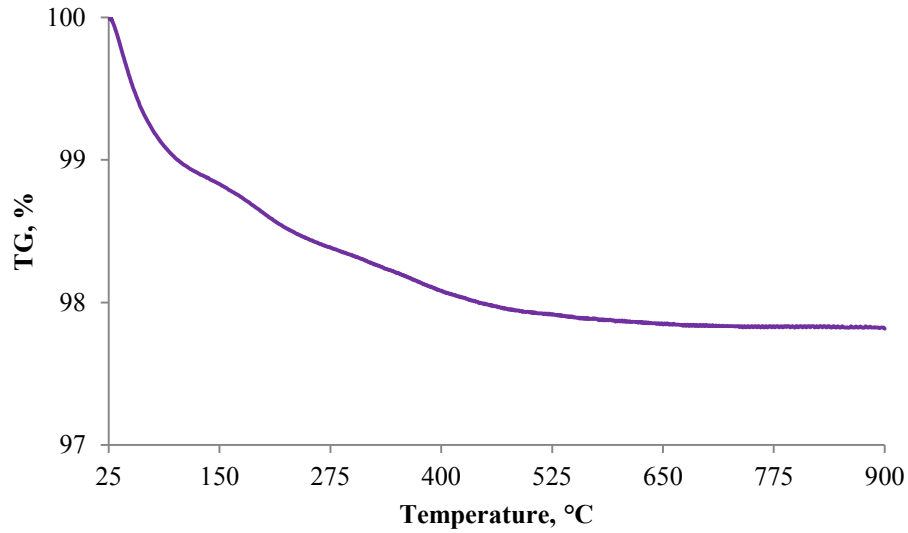

Fig. 13. TG curve of Fe_2O_3-TiO_2.

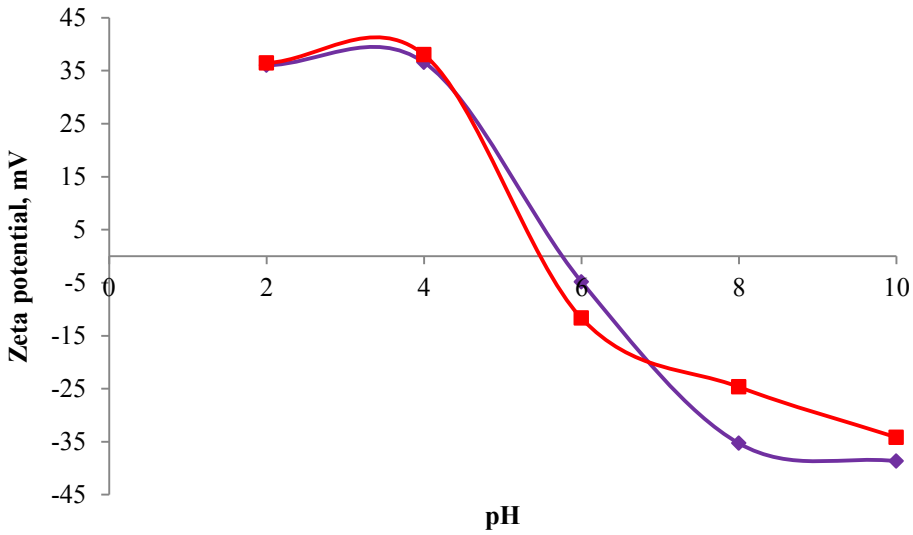

Fig. 14. Zeta potential curves of Fe_2O_3-TiO_2 (purple) and P25 (red).

Table 1

Experimental range and coded levels of initial pH (of the effluent), photocatalyst (Fe_2O_3-TiO_2) dosage, and air flow-rate.

Factors	Symbols		Coded levels				
	Actual	Coded	-1.682	-1	0	+1	+1.682
initial pH	X_1	x_1	3.23	3.50	3.90	4.30	4.57
photocatalyst dosage, g/L	X_2	x_2	0.5	0.7	1.0	1.3	1.5
air flow-rate, L/min	X_3	x_3	1.7	1.9	2.2	2.5	2.7

Table 2

Preliminary photocatalytic experiments.

Treatment	COD removal, %
Photolysis	0.1
Catalysis	0.4
Fe_2O_3-TiO_2	62.3
P25	40.6
Anatase TiO_2	24.9
Rutile TiO_2	2.9
Fe_2O_3	1.1

All treatments were conducted at initial pH = 4, [catalyst] = 1.5 g/L, air flow-rate = 4.0 L/min, irradiation duration = 3 h.

Table 3

ANOVA results of the quadratic models developed for COD removal from PPME using Fe_2O_3-TiO_2.

Source	Sum of squares	Degree of freedom	Mean square	*F* value	*p* value
Model	1829.94	9	203.33	324.69	< 0.0001*
x_1	13.80	1	13.80	22.03	0.0008*
x_2	1391.69	1	1391.69	2222.41	< 0.0001*
x_3	37.97	1	37.97	60.64	< 0.0001*
x_1^2	203.34	1	203.34	324.71	< 0.0001*
x_2^2	30.64	1	30.64	48.93	< 0.0001*
x_3^2	118.90	1	118.90	189.88	< 0.0001*
$x_1\ x_2$	3.12	1	3.12	4.99	0.0495*
$x_1\ x_3$	0.13	1	0.13	0.20	0.6646
$x_2\ x_3$	78.12	1	78.12	124.76	< 0.0001*
Lack-of-fit	3.43	5	0.69	1.21	0.4197
Pure error	2.83	5	0.57		

R^2 = 0.9966, adjusted R^2 = 0.9935, adequate precision = 67.16

*significant terms where *p* values < 0.05

Table 4

Textural properties of fresh and reused Fe_2O_3-TiO_2, P25, and Fe_2O_3.

Sample	Surface analysis		
	Specific surface area, m^2/g	Pore volume, cm^3/g	Pore size, nm
P25	52.32	0.17	15.62
Fe_2O_3	17.45	7.70	0.03
Fresh Fe_2O_3-TiO_2	58.40	0.29	18.52
Reused Fe_2O_3-TiO_2			
Cycle			
1	55.77	0.27	18.42
2	54.10	0.26	18.37
3	52.60	0.26	18.21
4	51.44	0.26	17.95
5	50.81	0.25	17.16

Table 5

Magnetic properties of fresh and reused Fe_2O_3-TiO_2.

Sample	Saturation magnetization (M_s), emu/g	Coercivity (H_{ci}), Oe	Remnant magnetization (M_r), emu/g
Fe_2O_3*	58.56	330.37	16.70
Fresh Fe_2O_3-TiO_2	5.23	27.96	0.17
Reused Fe_2O_3-TiO_2 after 5 cycles	1.95	11.56	0.15

* literature values obtained from Jayanthi et al. [52]